The Meteoritical Society

Meteoritics & Planetary Science 1–13 (2017)
doi: 10.1111/maps.12853

On the depths and shapes of the freshest kilometer-scale simple craters on the lunar maria: A new crater shape model

J. E. CHAPPELOW*

Meteorifics Inc., 1148 Sundance Loop, Fairbanks, Alaska 99709, USA
*Corresponding author. Email: john.chappelow@saga-inc.com

(Received 09 November 2016; revision accepted 06 February 2017)

Abstract–Recent work on the shapes of small, simple impact craters on the Moon has shown that the parabolic ideal does not well represent the vast majority of these craters. They are hyperbolic in shape and usually resemble a cone more than a parabola. A parabolic shape also does not fit the most commonly held archetype for simple craters in general (Linné), which is also hyperbolic. In addition, Linné itself may not be the best model for fresh simple craters, in terms of cross-sectional shape, although shape data to compare it to have heretofore been lacking. Here, the "free shadowfront method" for determining the shapes of simple craters is used to measure 64 fresh simple craters on five lunar maria to test both assumptions. Laser altimetry cross sections, available for many of the craters measured herein, are used to complement and spot-check the shadow measurement results, and thereby demonstrate the efficacy of the free shadowfront method. A new shape model is established, and two craters that better fit this model than Linné are identified. These are located at 24.45° N/328.12° E and 31.35° N/296.46° E and have diameters of 1.40 and 2.73 km, respectively. An apparent dichotomy between fresh simple craters smaller than 2.5 km and those larger than this is observed. Flat floors are found to be ubiquitous among the larger craters, but rare and small in extent in smaller ones. A slide in one crater which appears to be an incipient flat floor suggests a major mode of formation for these flat floors.

INTRODUCTION

The shapes of impact craters reflect the properties of the impacting objects and the surfaces they strike, the dynamics of their formative impact events, their ages and the processes which modify them, and the bodies on which they are formed. A crater's shape can control the thermal and radiative environment within it, and thus whether or not it may contain deposits of volatiles. Also, results from experimental and computational studies of crater formation must be validated to the shapes of real craters. Understanding the precise shapes of impact craters is therefore of considerable scientific interest.

The existing shape model for small, simple craters is that they are approximately parabolic and have depths (d) of about one-fifth of their diameters (D) (Wilhelms et al. 1987; Melosh 1989, 2011; DePater and Lissauer 2001). This parabolic model is commonly used for a variety of purposes (e.g., Settle and Head 1979; Vogler et al. 1991; Veverka et al. 2001; Robinson et al. 2002; Giese et al. 2006; Salamunićcar et al. 2012; Bland 2013; and others) and has become embedded in planetary science. Yet it has been shown to be rather inaccurate. Using shadow measurements, Chappelow (2014, 2015) found that most simple craters on Mare Serenitatis are shallower than $d/D = 0.2$, and are hyperbolic rather than parabolic—a shape intermediate between a parabola and a cone.

The current type example of a simple crater is Linné crater on the Moon, and it appears as an example in several references and texts (e.g., Taylor 1982; Wilhelms et al. 1987; Melosh 1989, 2011; Hargitai and Watters 2014), and numerous publications. Uncratered, with a sharp rim, well-defined ejecta features, and bright halo of ejecta, Linné is obviously a

very fresh, apparently unmodified simple crater. However, using both stereogrammetry and gridded laser altimetry Garvin et al. (2011) found that Linné crater contains a flat bottom, is shaped like "truncated cone," and is best fit by a power law with an exponent placing it again between parabolic and cone shaped. Using shadows, Chappelow (2013) also showed that Linné is hyperbolic in form. Thus, the current model for simple craters is rather inaccurate, and Linné as its paradigm questionable.

The central purpose of the work presented here is to formulate a new model for young, fresh, simple craters that more accurately reflects their true shapes yet is still mathematically compact, intuitive, and easy to use. To do this I have determined the shapes and dimensions of several dozen (66) fresh, young, simple craters on the lunar maria using the free shadowfront method (FSM) of crater measurement (Chappelow 2013). The new model will also provide a valuable benchmark for comparison with other craters—those formed under different conditions (e.g., secondaries), into different targets (e.g., lunar highlands) and bodies (e.g., Mercury), and/or which have been modified by physical processes (e.g., more ancient lunar maria craters).

As it is a relatively new technique, another important goal of this work is to describe the current state of the FSM and demonstrate its application and usefulness. These results will be supplemented with, and compared to, laser altimetry data available for many of the craters studied herein.

METHODS

The Free Shadowfront Method

Previously, Chappelow (2013) has shown that the "free shadowfront," that part of the shadow boundary not coincident with the crater rim, in a crater with a cross-section shaped like a geometric conic section (i.e., elliptical, parabolic, hyperbolic, or conical), must itself be a segment of an ellipse. This was designated the "shadowfront ellipse" (SFE). In addition to being elliptical, one axis of the SFE must lie along the "illumination axis" (the horizontal axis pointing from the crater center in the direction of the solar azimuth), and the other, transverse, axis must be of length D (Fig. 1). It was also shown that the crater shape-related quantities d, the rim-to-bottom depth, and e, the eccentricity of the crater's conic sectional cross section, can be analytically related to the directly measurable quantities R, the crater radius, α, and x_c (see Fig. 1 for definitions) associated with the SFE. They are related via the equations:

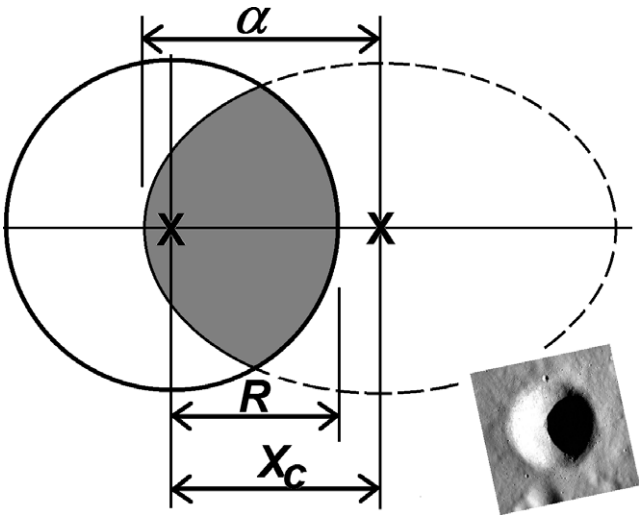

Fig. 1. Definitions of measurable quantities associated with the shadowfront ellipse (SFE; dashed ellipse) and the crater rim (solid circle). Centers of the crater and the SFE are marked X, the shadow is in gray, and the illumination is from the right. Inset: An example crater shadow analyzed in this work, for comparison.

$$d = \frac{(\sqrt{R^2 - \alpha^2 + x_c^2} - x_c)}{(R - \alpha)\tan\theta} R \tag{1}$$

and:

$$e = \sqrt{1 - \left(\frac{R - \alpha}{R + \alpha}\right)\tan^2\theta} \tag{2}$$

where θ is the solar incidence angle. Thus, a crater's depth and shape may be calculated by measuring R, α, and x_c and plugging them into Equations 1 and 2, and $D = 2R$; and without any requirement that the shadow tip lie at the crater center.

For practical purposes, the FSM has been implemented as a computer program, called CRATERZ. In its original form (Chappelow 2013), CRATERZ asked the user to select three, well-spaced points on the crater rim (the "rim points") followed by two more on the shadowfront (the "SFE points"), which are sufficient to fix both the rim circle and the SFE. (Note: while five independent quantities are generally required to fix an ellipse in a plane, the three constraints on the SFE mentioned above reduce this to only two.) To avoid computational problems the two SFE points cannot be located symmetrically about the illumination axis, and best results were obtained when one point was placed near, but not at, the shadow tip and the other near, but not on, the crater rim on the opposite side.

However, practical experience has shown that the required asymmetric placing of the SFE points introduces a bias; the resulting SFE tends to fit the section of the shadowfront between the two SFE points and ignore the rest. In addition, selecting only three rim points similarly tends to emphasize only those three points, and not fit the entire rim. To alleviate this, the current iteration of CRATERZ lets the user choose any number of points (greater than the minimums) and then fits a circle to the rim points and an ellipse to the SFE points using least squares routines. This greatly reduces the effects of subjectivity in selecting the points, and greatly improves precision (in the statistical sense). Practice has shown that specifying seven rim points and nine SFE points strikes a good balance; using more points takes more time and rarely results in significantly better precision in the measurements of R, α, and x_c.

A Relevant Example: Linné Crater

Chappelow (2013) included an analysis of Linné crater using Lunar Reconnaissance Orbiter (LRO) Wide Angle Camera (WAC) image m162229369 (pixel scale 56.2 m/pix). More recently, LRO_NAC image m1184753661r with approximately 45× better resolution (pixel scale 1.27 m/pix) became available, and the same procedure was performed on this image. For convenience, the NAC image was actually downsampled by a factor of 4×, making the final pixel scale 5.08 m/pix. Ten trials of the FSM were performed on a clip of Linné from the NAC image and the results for D, d, and e averaged. The output screen from an example trial is shown in Fig. 2, and shows the placement of the rim and SFE points and the circle and ellipse fitted to them; both sets of results are tabulated in Table 1. Both compare well with the results of the LOLA laser altimetry and stereogrammetry-derived digital terrain model (DTM) described in Chappelow (2013). Linné's cross sectional shape and dimensions are shown in Fig. 3, and a comparison with a nearly center-crossing LOLA track in Fig. 4. These results show that Linné is deeper than the familiar $d/D = 0.20$, and is neither parabolic nor conical (see Fig. 5), and motivate the effort to find a new paradigm for fresh, simple craters.

Beyond confirming the earlier results, these newer, nearly identical results illustrate one of the strengths of the FSM: Within limits, it is quite insensitive to image resolution compared to other image-based methods (stereogrammetry, photoclinometry). It is also relatively insensitive to albedo and illumination variations, shadows due to small-scale topography or surface roughness, image noise, and atmospheres. Images need not even be photocorrected, requiring at most a quick histogram stretch to bring out and sharpen the crater rim and the shadowfront. However, it also highlights that, like any shadow method, the FSM cannot account for any crater features which may be hidden within the shadow (e.g., flat bottoms). Thus, by itself, the best it can do is set upper limits on the flat bottom Linné is known to contain, unless the shadow was to cross the flat bottom. Using the shadow length (L = 1383 m) and the solar incidence angle (θ) it is easy to calculate the maximum thickness ($T_{ff} = d - L/\tan\theta \approx 53$ m) and radius ($R_{ff} = L - R \approx 290$ m) of any flat floor which might be hidden in Linné's shadow (Fig. 2 illustrates this graphically). Note in Fig. 3 that Linné's T_{ff} is actually much smaller at ~20 m. Thus, it is still advantageous to use crater images with shadows as close to the crater center/bottom as possible. Then, if any part of the flat bottom is illuminated, including it in the crater shape is simple (Chappelow and Sharpton 2002; Chappelow 2013).

Selecting and Analyzing the Craters

The primary objective herein is to develop a model for simple craters which are as close to their initial states as possible and unaffected by other factors such as pre-existing topography or target inhomogeneities. This leads naturally toward utilizing the lunar maria as a "test plate"; they are some of the smoothest, most homogeneous surfaces in the solar system, with the added benefit that they are now well-covered by high-resolution imagery, courtesy of the LRO's Narrow Angle Camera (NAC). In addition, the freshest craters are relatively easy to identify, as their bright interiors and ejecta contrast sharply with the dark surfaces of the lunar maria.

Along with sharp rims, well-defined ejecta features, and relatively uncratered interiors and ejecta blankets, the presence of optically bright interiors, rays, and halos of ejecta have long been recognized as diagnostic of fresh, unmodified simple impact craters (e.g., Pohn and Offield 1970; Head 1975; Wilhelms et al. 1987; Melosh 1989; and others). In a sample of over 100 simple craters on Mare Serenitatis, Chappelow (2015) found several which retained many of these features (and which had deepnesses, $d/D > 0.23$), yet which had lost any bright ejecta halos they must once have had. This implies that these bright ejecta halos are the first distinguishing features that small, pristine craters on the Moon lose (see also Pohn and Offield 1970; Head 1975; Werner and Medvedev 2010). Therefore, the presence of such a bright ejecta halo is taken here as indicative of the freshest of fresh craters on the Moon, and a primary criterion for selection into this study. Henceforth,

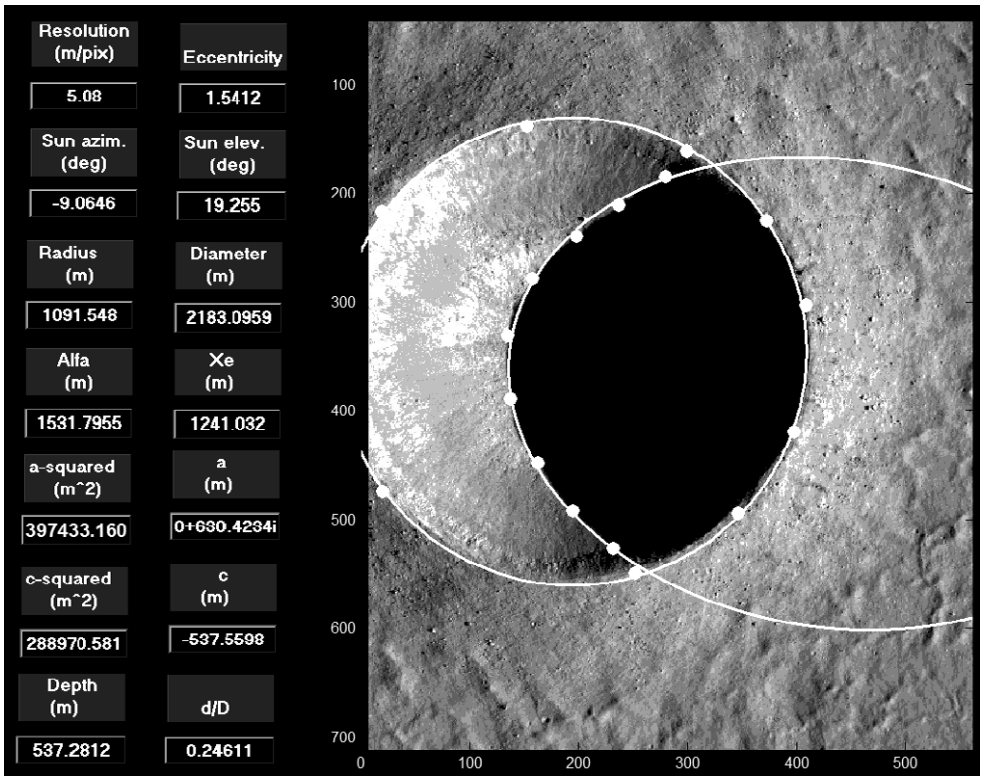

Fig. 2. Output screen from a sample trial measurement of Linné showing the user defined rim- and shadowfront ellipse (SFE)-points and the rim circle and shadowfront ellipse fitted to them.

Table 1. Summary of results for Linné crater.

Image ID	WAC m162229369	NAC m1184753661r
Pixel scale	56.2 m/pix	5.08 m/pix
Emission angle	1.13°	1.19°
Incidence angle	75.30°	70.73°
Diameter	2210.5 m (3σ = 61 m)	2181.0 (3σ = 16 m)
Depth	538.9 m	537.0 m
Eccentricity	1.517	1.520
d/D	0.244	0.246

fresh appearing craters with bright halos are termed "BHCs" while ones without a bright halo are simply referred to as "fresh craters."

Once identified, useful imagery of the BHCs must be found, and this involves several more qualifications: The crater must be imaged at a high enough resolution (minimum 50 pixels/diameter), from near the zenith (emission angle, <5°), and with appropriate solar illumination (63°θ 83°). And finally, it must satisfy the assumptions implicit in the FSM: It must have an approximately circular, continuous, even, and horizontal rim and smooth elliptical shadow shape consistent with a conicoidal interior shape. However, minor deviations from these conditions are not disqualifying—small craters or gaps in the rim or slides in the interior are not difficult to work around with the FSM (and below a shape is obtained even for a crater containing a large slide).

RESULTS

Under the above criteria 87 BHCs were identified on five lunar maria (Crisium, Imbrium, Procellarum, Serenitatis, and Tranquilitatis), of which 66 were successfully analyzed using the FSM. Most of the remainder BHCs produced unphysical results or their shadowfronts could not be well fit with an ellipse, both indicating that their shapes were not sufficiently conic section-like to satisfy the FSM. The diameter, depth, and eccentricity data are collected in Table 2, and are plotted in Figs. 5–7.

Two outliers are apparent at upper left in Fig. 5; their values for d/D and e are more consistent with more aged craters than with BHCs (Chappelow 2015). Re-examination revealed that these are not in fact BHCs—they appear so due to topographic and illumination effects. They are located on higher terrain (including one atop a wrinkle ridge), the slopes of which appear bright under solar illumination. Both were

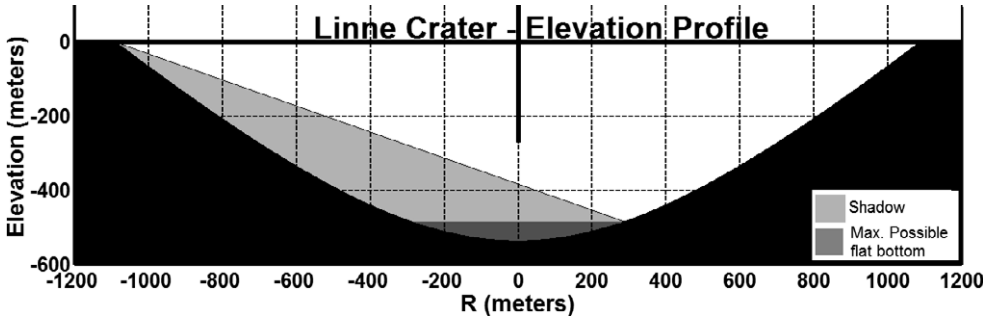

Fig. 3. A to-scale diagram of the results of measurement of Linné. The dark gray area is the maximum possible extent of Linné's shadowed flat bottom.

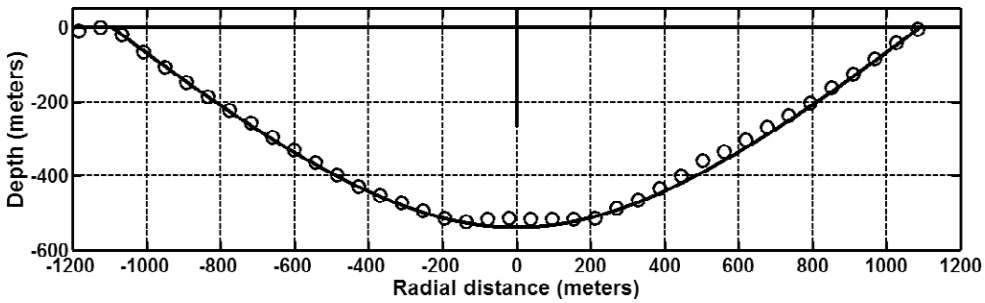

Fig. 4. Comparison of the free shadowfront method (FSM)-derived profile of Linné with a LOLA profile taken during LRO orbit 3132. Note the true size of Linné's flat bottom.

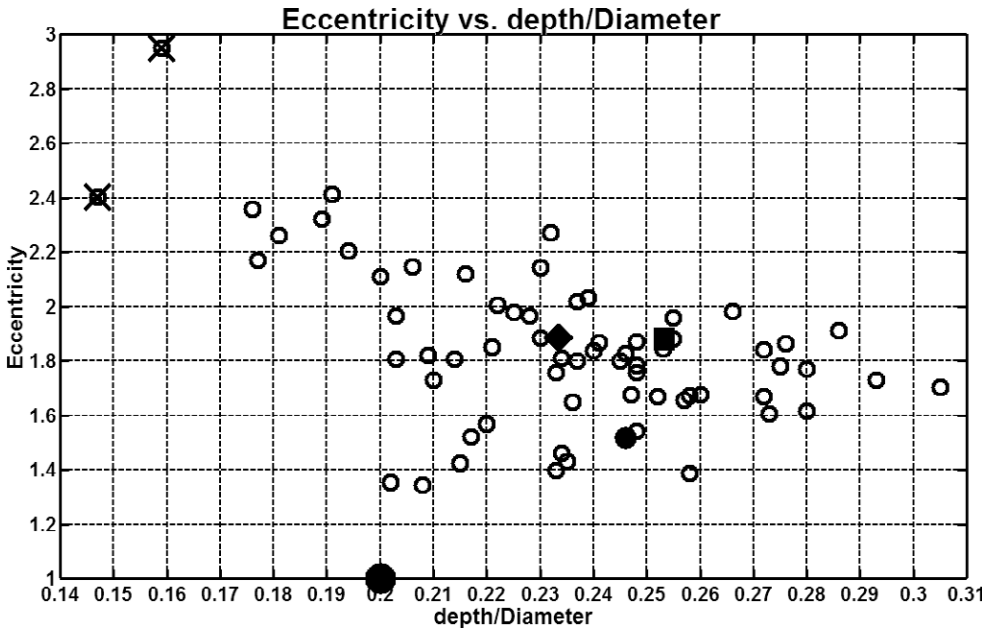

Fig. 5. A plot of eccentricity (e) versus deepness (d/D) for 66 presumed BHCs. Linné is marked in solid black and the current model for fresh simple craters is the larger black symbol at bottom. Two outliers at upper left were found not to be BHCs. The diamond symbol and square symbols mark the model results for $D < 2.5$ km and $D > 2.5$ km craters, respectively.

eliminated from the sample population based on these observations. Re-examination of six more BHCs with $d/D < 0.20$ found no other such examples.

Nearly bisecting LOLA data were also available for 28 of the remaining 64 BHCs and comparisons with the FSM are displayed in Fig. 8.

Table 2. Data for 64 bright halo craters (BHCs). T_{ff} and d_{ff} are the thickness and rim-to-floor depth of the craters flat floors, respectively

Crater#	Lat (°)	Long (°)	D (m)	d (m)	ecc	d/D	T_{ff} (m)	d_{ff} (m)	d_{ff}/D
mbh085	46.83	−52.13	6856	1697	1.872	0.248	236	1461	0.213
mbh066	−0.59	24.18	5777	1386	1.836	0.240	77	1310	0.227
mbh080	40.89	−50.83	5659	1334	1.648	0.236	90	1244	0.220
mbh020	33.25	−61.52	4824	1242	1.387	0.258	146	1097	0.227
mbh062	38.16	−17.32	4155	1022	1.828	0.246			
mbh017	32.63	−25.05	3806	1115	1.729	0.293	261	854	0.224
mbh077	25.00	−77.78	3172	683	2.118	0.216			
mbh096	15.41	−48.31	3119	794	1.959	0.255	87	707	0.227
mbh059	39.38	−13.98	3070	847	1.863	0.276	215	633	0.206
mbh014	36.51	−6.93	2973	833	1.769	0.280	102	732	0.246
mbh073	31.35	−63.54	2734	697	1.880	0.255			
mbh097	−4.63	−39.11	2661	541	1.806	0.203	71	470	0.177
mbh078	25.58	−64.84	2566	734	1.910	0.286	134	601	0.234
mbh034	43.49	−0.44	2450	434	2.170	0.177			
mbh004	33.64	23.02	2418	599	1.782	0.248			
mbh015_1	42.26	−19.77	2207	557	1.845	0.253			
mbh098	27.74	11.8	2181	536	1.518	0.246	20	517	–
mbh023	44.6	−24.61	2166	521	1.866	0.241			
mbh060	12.66	56.77	2166	486	1.978	0.225			
mbh005	30.03	24.91	1990	511	1.654	0.257			
mbh070	−6.18	49.57	1948	529	1.669	0.272	29	500	–
mbh010	21.65	26.99	1864	496	1.980	0.266			
mbh091	24.66	−57.93	1864	484	1.677	0.260			
mbh089	26.37	−66.1	1855	566	1.703	0.305			
mbh087	38.7	−69.02	1819	425	1.810	0.234			
mbh016	35.41	−29.99	1760	414	1.430	0.235			
mbh071	39.79	−53.19	1664	365	1.568	0.220			
mbh042	43.75	−24.94	1571	371	2.018	0.237			
mbh093	9.86	−48.31	1525	392	1.671	0.258			
mbh095	16.15	−61.47	1498	377	1.670	0.252	32	345	–
mbh024	45.77	−23.68	1430	269	2.321	0.189			
mbh092	3.95	−47.97	1417	330	1.757	0.233			
mbh007	20.23	14.69	1400	299	1.806	0.214			
mbh054	24.45	−31.88	1398	321	1.885	0.230			
mbh076	30.01	−71.87	1376	289	1.729	0.210			
mbh011	29.4	23.72	1321	272	2.147	0.206	22	250	–
mbh079	24.99	−64.7	1316	325	1.756	0.248			
mbh090	13.47	−61.3	1294	362	1.616	0.280			
mbh032	32.03	6.01	1270	348	1.78	0.275			
mbh009	19.73	24.4	1253	342	1.605	0.273			
mbh026	45.26	−11.71	1248	252	1.966	0.203			
mbh030_1	21.55	20.76	1209	276	1.964	0.228			
mbh021	32.11	−31.87	1190	293	1.677	0.247			
mbh084	50.43	−47.73	1123	258	2.144	0.230			
mbh056	17.00	−23.33	1086	294	1.842	0.272			
mbh013	24.06	9.24	1050	245	1.461	0.234			
mbh008	21.14	14.74	1048	244	1.397	0.233	25	219	–
mbh053	23.92	−32.44	1047	248	1.800	0.237			
mbh050	34.98	−29.85	1033	224	1.520	0.217			
mbh022	43.62	−28.76	984	212	1.422	0.215			
mbh047_1	40.02	−25.14	955	211	1.850	0.221			
mbh082_1	45.32	−55.42	948	226	2.033	0.239			
mbh019	26.6	−26.71	937	232	1.542	0.248			

Table 2. *Continued*. Data for 64 bright halo craters (BHCs). T_{ff} and d_{ff} are the thickness and rim-to-floor depth of the craters flat floors, respectively.

Crater#	Lat (°)	Long (°)	D (m)	d (m)	ecc	d/D	T_{ff} (m)	d_{ff} (m)	d_{ff}/D
mbh029	27.22	15.4	900	208	2.271	0.232			
mbh018	27.07	−24.35	862	180	1.819	0.209			
mbh003	34.46	12.76	811	168	1.344	0.208	30	139	–
mbh001	36.51	14.26	795	176	2.005	0.222			
mbh058	48.84	−17	793	151	2.411	0.191			
mbh033	42.39	0.98	738	181	1.799	0.245			
mbh044	44.06	−24.57	676	135	2.108	0.200	7	128	–
mbh002	34.85	13.23	663	133	1.352	0.202			
mbh040	45.23	−23.54	657	115	2.359	0.176			
mbh045	44.88	−26.28	594	115	2.203	0.194			
mbh036	50.53	−16.45	582	105	2.261	0.181			

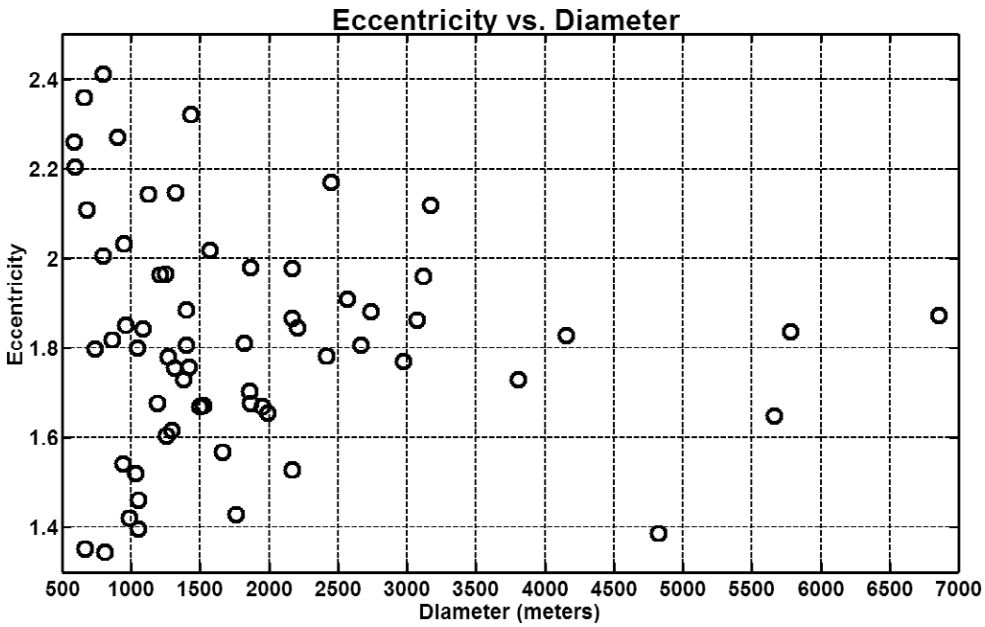

Fig. 6. Eccentricity versus diameter for 64 bright halo craters (BHCs).

Analysis

Figures 6 and 7 and Table 2 all suggest a dichotomy in the craters' shapes and shape distributions. Figure 6 indicates that BHCs smaller than $D \approx 2.5$ are considerably more variable in the eccentricity parameter than larger ones. In the larger craters, e is confined essentially to the range 1.6–2.2, while for the smaller craters this range is 1.3–2.4. Figure 7 and Table 2 (which is sorted by crater diameter) show that most of the larger BHCs contain extensive flat floors (10/13) while these are rare and small-to-negligible in the smaller ones (7/51). These observations lead to the treatment of these two groups of BHCs separately.

Interestingly, the flat floors in the larger BHCs tend to reduce their depths in such a way as to cluster their deepnesses roughly within the range $0.21 \leq d/D \leq 0.23$. And of the three without flat bottoms, mbh077 has $d/D = 0.216$ without a flat floor, and mbh062 has a large anomalous feature which may be a slide, constituting an incipient flat floor (see the crater mbh062).

The New Model

The model for both size ranges of BHCs was assembled by normalizing (scaling) the FSM profiles to $R = 1$, sampling them at 201 points across their diameters, then stacking and averaging them point by point, yielding a normalized, averaged profile for each

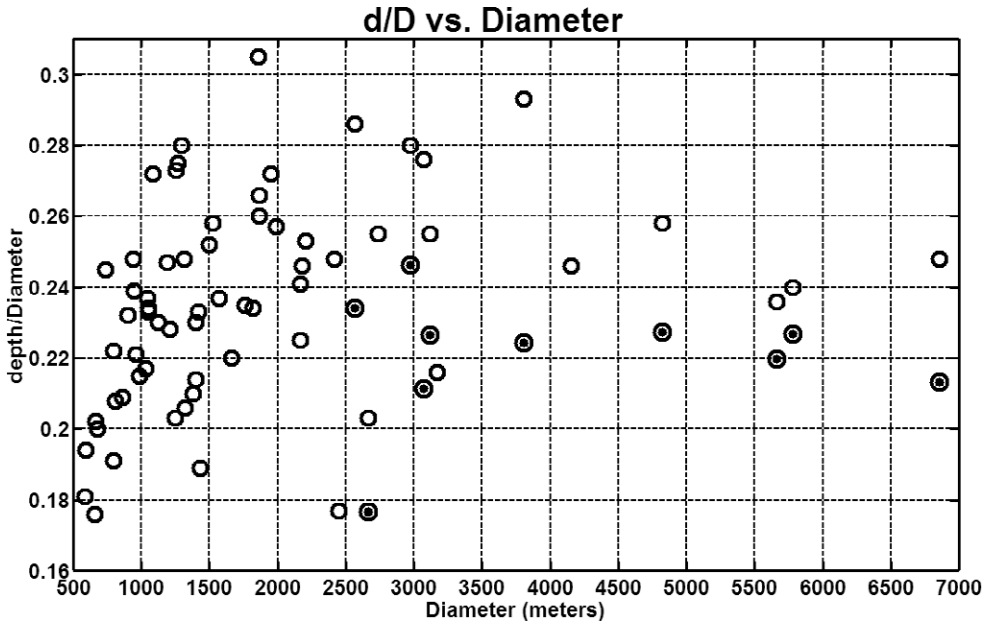

Fig. 7. Deepness versus diameter for 64 bright halo craters (BHCs). The bull's-eye symbols directly below most of the larger ($D > 2.5$ km) craters represent their deepnesses (d/D) with their flat floors included.

class (small, large) of BHCs separately. Parameters a^2 and c for the approximating conics represented by these two average profiles were obtained by evaluating their algebraic equation:

$$\frac{r^2}{a^2} + \frac{(z-c)^2}{c^2} = 1 \tag{3}$$

(where z is the elevation above the crater bottom and r the radial distance from its symmetry axis; see Chappelow 2013) at two points (r_i, z_i) taken from the profiles and solving the resulting simultaneous equations. Together with the normalization condition, $R = 1$, these fully specify the crater models' shapes and dimensions. The results are summarized in Table 3. The eccentricity was then calculated from its definition:

$$e = \sqrt{1 - \frac{a^2}{c^2}} \tag{4}$$

for convenient comparison with FSM results.

For practical purposes, the general expression for the crater shape conic [3] can be rearranged into the functional form:

$$z(r) = c - c\sqrt{1 - \frac{r^2}{a^2}} \tag{5}$$

which gives the elevation of the crater interior surface as a function of radial distance from the bottom/center of the crater interior; plugging c and a^2 into this produces the algebraic model for the BHCs. However, it is important to remember that c and a^2 are normalized to $R = 1$; therefore, they must be multiplied by R and its square (respectively) to represent the true shape and dimensions of a crater of radius R. Carrying this out, for the smaller BHCs:

$$z(r) = -0.236R + 0.236R\sqrt{1 + \frac{r^2}{0.127R^2}} \tag{6}$$

or in terms of the more commonly used diameter, D, instead of radius:

$$z(r) = -0.118D + 0.118D\sqrt{1 + 31.400\frac{r2}{D^2}} \qquad (0.5\text{km}\, D \leq 2.5\text{km}) \tag{7}$$

The corresponding expression for the larger ($D > 2.5$ km) BHCs is:

$$z(r) = -0.087D + 0.087D\sqrt{1 + 56.794\frac{r^2}{D^2}} \qquad (2.5\text{km}\, D \leq \sim 7\text{km}) \tag{8}$$

Practical experience with the FSM suggests an error estimate of ~1% in the diameter measurement when applied to craters larger than ~30 pixels across in typical LRO_NAC images (see Table 1).

Together Equations 7 and 8 constitute the new model for the freshest craters on the lunar maria (BHCs) with diameters 0.5 km $\leq D \leq$ ~7 km. Figure 9 shows that they represent very similar hyperbolic shapes

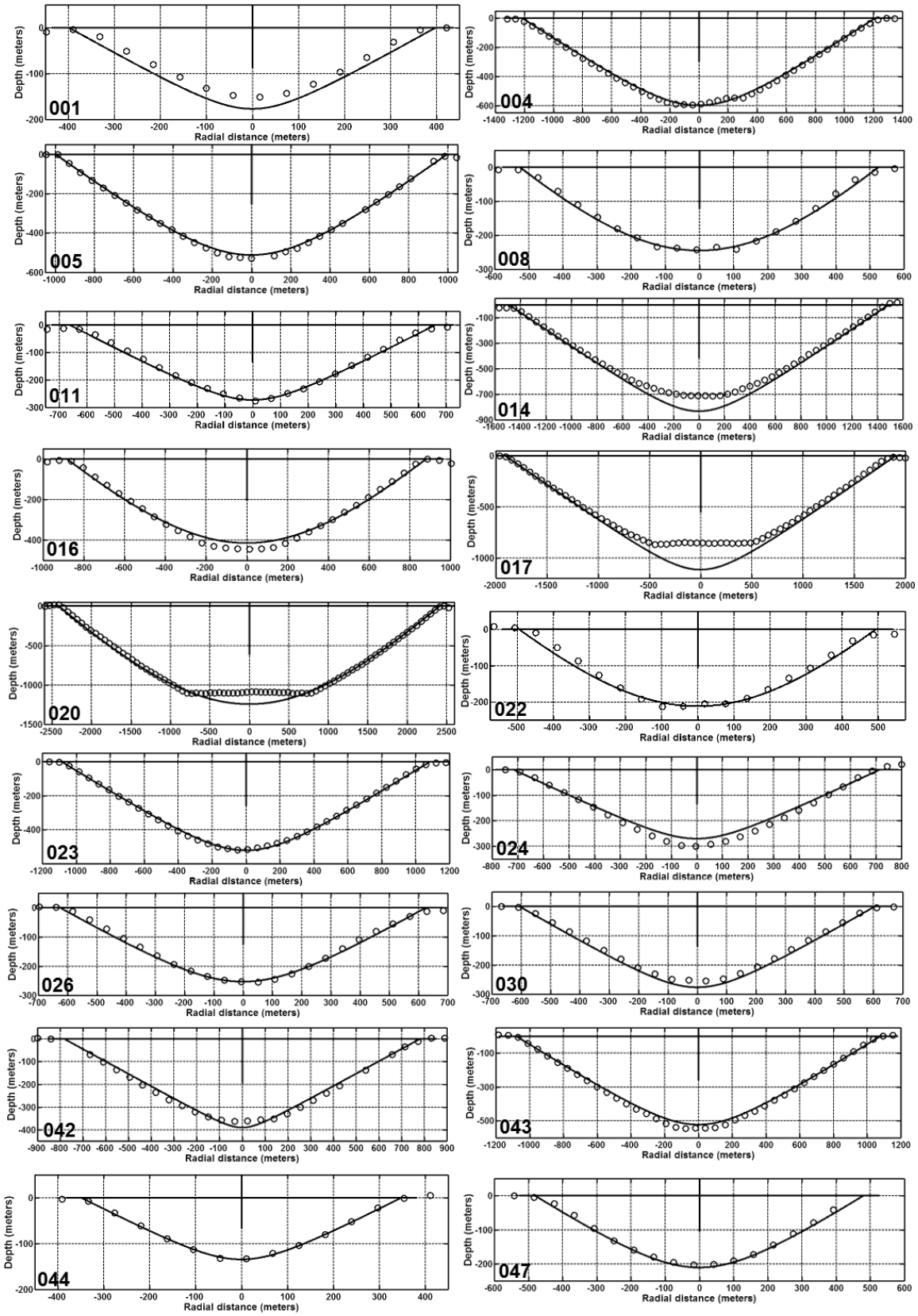

Fig. 8. Comparisons of free shadowfront method (FSM) results (solid curves) with LOLA transect data. Large flat floors occur in almost all of the examples larger than 2.5 km in diameter. The LOLA track in mbh001 was significantly off-center.

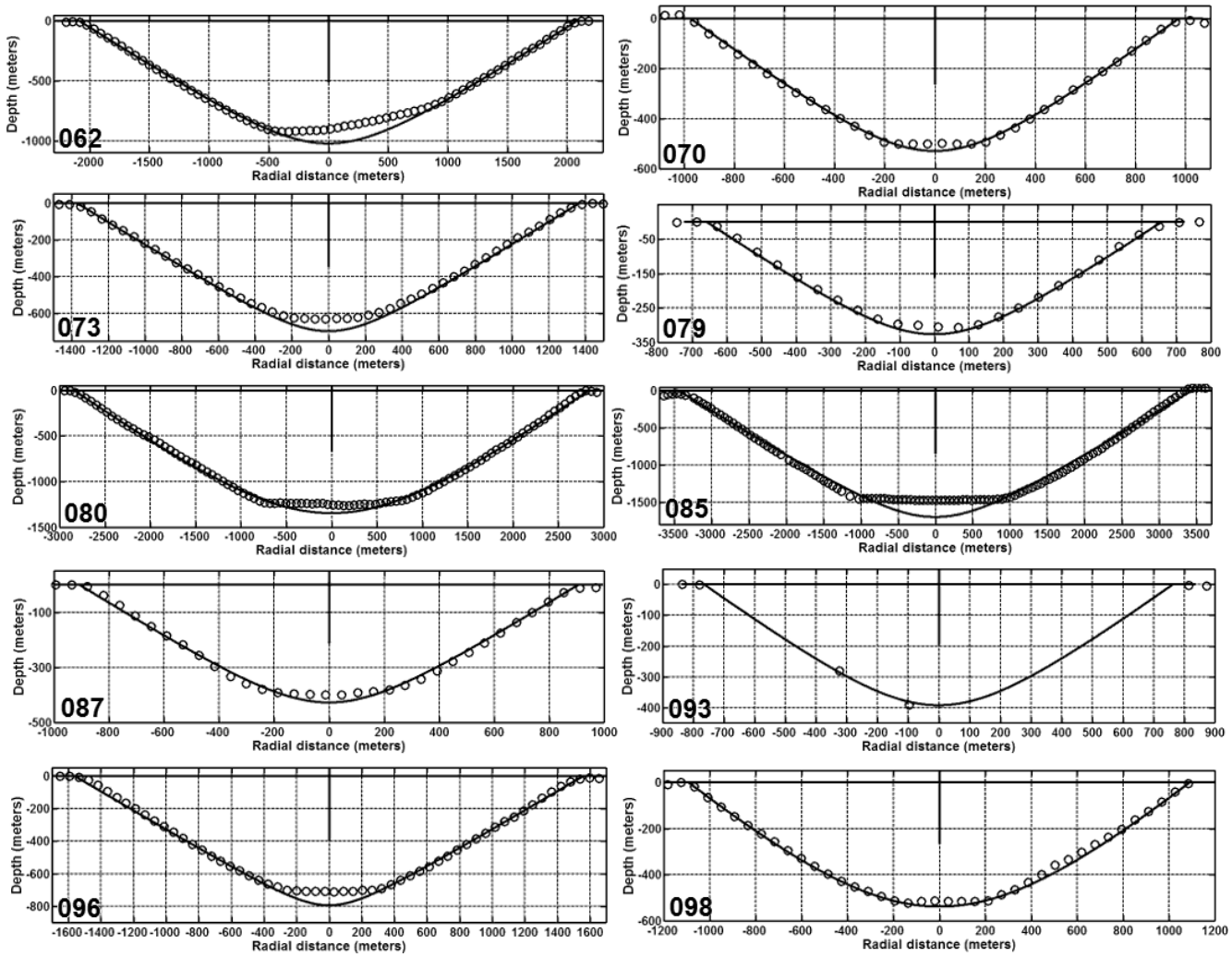

Fig. 8. Continued.

Table 3. Normalized model crater shape parameters.

	Small BHCs	Large BHCs
a^2	−0.12739	−0.07043
c	−0.23582	−0.17466
d/D	0.233	0.253
e	1.893	1.875

and are qualitatively more cone-like than parabolic. In fact, the similarity in their e values suggests that the apparent difference in eccentricity noted above may well be due to the small number of the larger BHCs sampled (n = 13). But the deepness (d/D) difference is not as easy to dismiss, and may be due to modification processes shallowing the smaller BHCs proportionally more than the larger ones, without affecting their shapes. The difference in numbers and sizes of flat floors between the two populations also appears real; flat floors are common among the larger BHCs, but relatively rare and minor at smaller diameters, in general. The reason for this is unknown, and is beyond the intended scope here. However, they are too varied in extent and in the presence/absence to be included quantitatively in the model, except to note that they tend to result in final depth-diameter ratios of 0.21–0.23 (Fig. 7). Data on their dimensions are provided in Table 2.

As a last step, the two craters closest to the new model shapes, and which therefore better represent lunar simple craters than does Linné, were identified in Fig. 5 and looked up in Table 2. The crater which best represents the smaller BHCs is mbh054 located at 24.45° N 328.12° E and has a diameter of 1.40 km, and that which best represents the larger BHCs is mbh073 located at 31.35° N 296.46° E and is 2.73 km in diameter. Both are shown in Fig. 10.

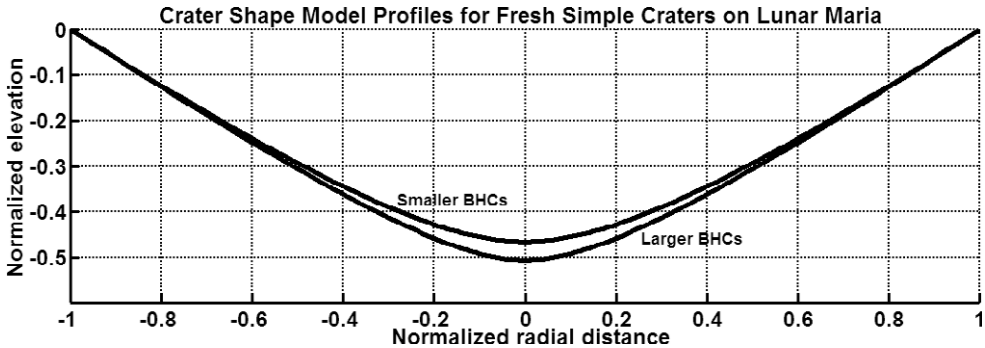

Fig. 9. A plot of the new model crater shape profiles. Note the similarity in shape.

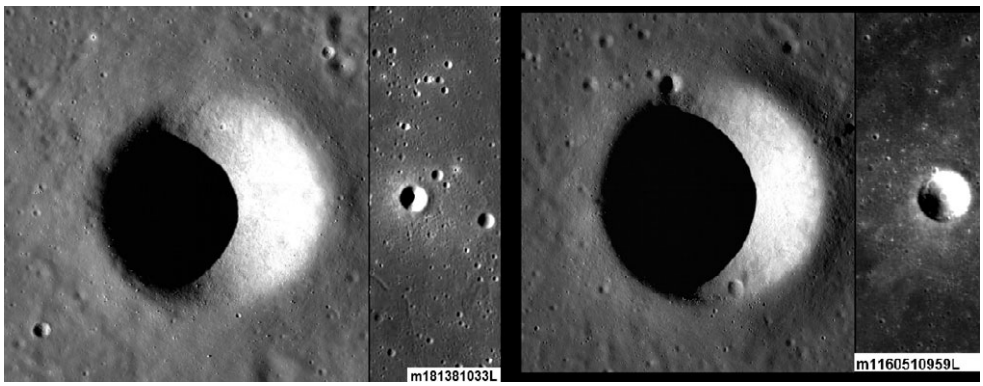

Fig. 10. Best examples of the new simple crater model: mbh054, D = 1.4 km (left) and mbh073, D = 2.7 km (right). The free shadowfront method (FSM) result for mbh073 is compared to a LOLA track in Fig. 8. Higher sun angle images are shown in insets.

Crater mbh062

The anomalous LOLA profile, and a small excursion in the shadowfront, of crater mbh062 (Fig. 11) prompted a closer examination. This crater is located at 38.16° N 342.68° E and has a diameter of 4.16 km. Inspection of LRO_NAC image m1134301807r, taken at a high enough illumination angle that no shadows were present, revealed a small, off-center, flat floor-like feature. The image was then draped over the crater shape determined earlier via FSM measurement (Fig. 12). Viewing this model from the southeast at an elevation angle of ~45° confirms that the anomalous feature is a large slide which has descended the north slope of the crater, flowed across the crater bottom, and continued a short distance up the opposite slope. It appears to represent an incompletely formed flat bottom, a conclusion supported by the fact that mbh062 is one of only three craters larger than 2.5 km in the sample population without a large, well-defined flat floor (yet). This implies that sliding/slumping is a major contributor to construction of such flat floors, and that such singular events contribute to this process and may even form flat floors in single events.

Finally, it is noteworthy that although this slide slightly altered the shape of the shadowfront in mbh062, it had little effect on the FSM measurement, which closely fit all of the crater's shape except the slide itself (Fig. 11).

CONCLUSIONS

Here, I have presented a new analytic model for fresh simple craters based on the shapes of 64, bright halo craters (BHCs) measured using the free shadowfront method. Due to an apparent qualitative difference in the shapes and shape distributions between smaller (D < 2.5 km) and larger (D > 2.5 km) BHCs, the model is presented in two parts (although it is important to note that the dichotomy in the eccentricity, e, may be due to the small sample size of the larger BHCs). Based on this new model, two craters more representative of the true shapes of simple lunar craters than Linné are also identified. Although it is founded upon the shapes of craters found on the lunar

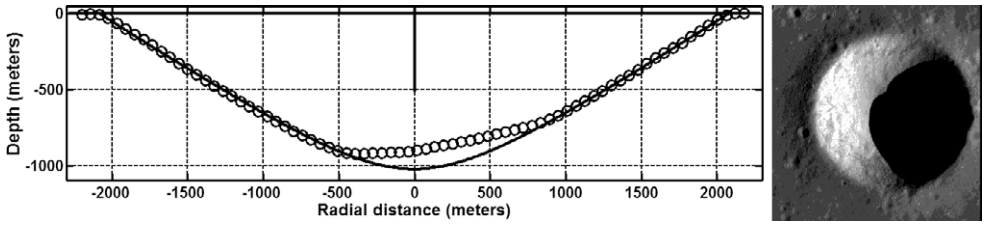

Fig. 11. The free shadowfront method (FSM) profile (solid line) and LOLA profile data bisecting crater mbh062 (left), and the image clip used to obtain the FSM profile (right). North is to the right in the graph, and toward the top in the image.

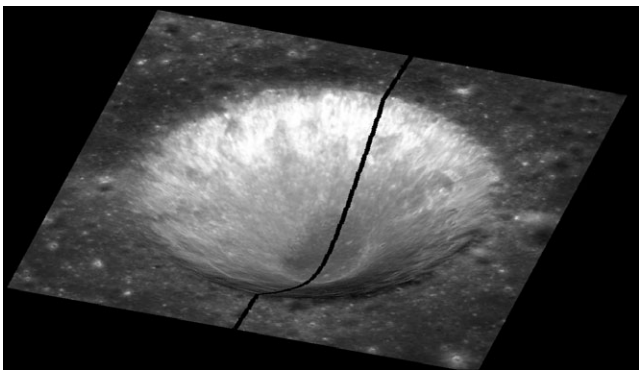

Fig. 12. A high-Sun, nadir-looking image of crater mbh062 projected onto the crater's shape as determined via the free shadowfront method (FSM) and showing the path of the LOLA transect shown in Fig. 11. The view is from the SSE from ~45° elevation.

maria, this new model may find application on other surfaces and bodies as well, like the current parabolic model.

The evident dichotomy between smaller and larger BHCs includes a substantial difference in the occurrence of flat floors within the craters: Most (10/13) of the larger BHCs host extensive flat floors, while few (7/51) were found in the smaller ones, and these were small to negligible in dimension. The seeming ubiquity of flat floors in the larger BHCs implies that they form soon after crater formation: The presence of bright ejecta halos about these craters, and a large slide in one of them that appears to be a flat floor in the process of formation, support this conclusion. It also suggests that sliding, slumping, and flowing of materials from the walls and pooling in the bottom may be a major contributor to the formation of flat floors. Retention of conic section-shaped cross sections, even in craters with large slides and flat floors, indicates that whatever the process of their formation it does not greatly affect these craters' hyperbolic shapes. Flat floors in the larger BHCs, and possible shallowing of the smaller ones, imply that some modification of simple crater shapes does occur even before their bright ejecta is darkened by space weathering.

Acknowledgments—The computer program CRATERZ is available by agreement only through the author. It is written in MATLAB 5.1.3 + toolboxes + customized routines, and may not function under later versions. The author acknowledges the time and efforts of J. Head and R. Craddock whose reviews undoubtedly improved this manuscript. This work was made possible by NASA Lunar Data Analysis Program Grant NNX15AR22G. It is dedicated to the memory of Joana Chappelow, who also made it possible.

Editorial Handling—Dr. Stuart Robbins

REFERENCES

Bland M. T. 2013. Predicted crater morphologies on Ceres: Probing internal structure and evolution. *Icarus* 226:510–521.

Chappelow J. E. 2013. Simple impact crater shape determination from shadows. *Meteoritics & Planetary Science* 48:1863–1872.

Chappelow J. E. 2014. The shapes of the Linné simple impact craters on the Moon Not parabolic (abstract #2074). 45th Lunar and Planetary Science Conference. CD-ROM.

Chappelow J. E. 2015. The shapes of simple impact craters on Mare Serenitatis (abstract #1079). 46th Lunar and Planetary Science Conference. CD-ROM

Chappelow J. E. and Sharpton V. L. 2002. An improved shadow measurement technique for constraining the morphometry of simple impact craters. *Meteoritics & Planetary Science* 37:479–486.

DePater I. and Lissauer J. J. 2001. *Planetary sciences*. New York: Cambridge University Press.

Garvin J. B., Robinson M. S., Frawley J., Tran T., Mazarico E., and Neumann G. 2011. Linné: Simple lunar mare crater geometry from LRO observations (abstract #2063). 42nd Lunar and Planetary Science Conference. CD-ROM.

Giese B., Neukum G., Roatsch T., Denk T., and Porco C. C. 2006. Topographic modeling of Phoebe using Cassini images. *Planetary & Space Science* 54:1156–1166.

Hargitai H. and Watters W. A. 2014. Simple crater. In *Encyclopedia of planetary landforms*, edited by Hargitai H. and Kereszturi A. New York: Springer. pp. 1939–1946.

Head J. W. 1975. Processes of lunar crater degradation: Changes in style with geologic time. *The Moon* 12:299–329.

Melosh H. J. 1989. *Impact cratering: A geologic process*. New York: Oxford University Press.

Melosh H. J. 2011. *Planetary surface processes*. New York: USA: Cambridge University Press.

Pohn H. A. and Offield T. W. 1970. Lunar crater morphology and relative-age determination of lunar geologic units—Part 1. Classification. US Geological Survey Professional Paper 700-C. Washington, D.C.: U.S. Government Printing Office. pp. 153–162.

Robinson M. S., Thomas P. C., Veverka J., Murchie S. L., and Wilcox B. B. 2002. The geology of 433 Eros. *Planetary & Space Science* 37:1651–1684.

Salamunićcar G., Lončarić S., and Mazarico E. 2012. LU60645GT and MA132843GT catalogues of Lunar and Martian impact craters developed using a crater shape-based interpolation crater detection algorithm for topography data. *Planetary & Space Science* 60:236–247.

Settle M. and Head J. W. 1979. The role of slumping in the modification of lunar impact craters. *Journal of Geophysical Research* 84:3081–3096.

Taylor S. R. 1982. *Planetary science: A lunar perspective*. Houston, Texas: Lunar and Planetary Institute.

Veverka J., Thomas P. C., Robinson M. S., Murchie S., Chapman C., Bell M., Harch A., Merline W. J., Bell III J. F., Bussey B., Carcich B., Cheng A., Clark B., Domingue D., Dunham D., Farquhar R., Gaffey M. J., Hawkins E., Izenberg N., Joseph J., Kirk R., Li H., Lucey P., Malin M., McFadden L., Miller J. K., Owen W. M. Jr, Peterson C., Prockter L., Warren J., Wellnitz D., Williams B. G., and Yeomans D. K.. 2001. Imaging of small-scale features on 433 Eros from NEAR: Evidence for a complex regolith. *Science* 292:484–488.

Vogler K. J., Johnson P. E., and Shorthill R. W. 1991. Modeling the non-grey-body thermal emission from the full Moon. *Icarus* 92:80–93.

Werner S. C. and Medvedev S. 2010. The lunar rayed-crater population—Characteristics of the spatial distribution and ray retention. *Earth and Planetary Science Letters* 295 (1):147–158.

Wilhelms D. E., McCauley J. F., and Trask N. J. 1987. The geologic history of the Moon. USGS Professional Paper 1348. Denver, Colorado: US Geological Survey. 302 p.